



## RESEARCH ARTICLE

# Multimodal system for optical biopsy of melanoma with integrated ultrasound, optical coherence tomography and Raman spectroscopy

Anatoly Fedorov Kukk<sup>1\*</sup>  | Di Wu<sup>1</sup> | Evelyn Gaffal<sup>2</sup> | Rüdiger Panzer<sup>3</sup> | Steffen Emmert<sup>3</sup> | Bernhard Roth<sup>1,4</sup> 

<sup>1</sup>Hannover Centre for Optical Technologies, Leibniz University of Hannover, Hannover, Germany

<sup>2</sup>University Hospital Magdeburg, Magdeburg, Germany

<sup>3</sup>University Medical Center Rostock, Rostock, Germany

<sup>4</sup>Cluster of Excellence PhoenixD (Photonics, Optics and Engineering - Innovation Across Disciplines), Hannover, Germany

## \*Correspondence

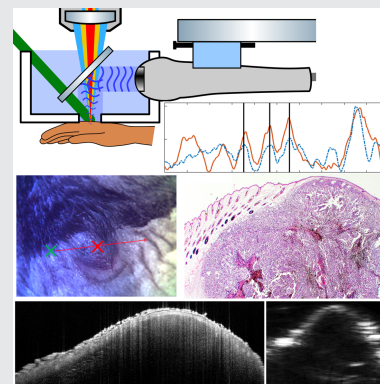
Anatoly Fedorov Kukk, Hannover Centre for Optical Technologies, Leibniz University of Hannover, Nienburger, Straße 17, 30167 Hannover, Germany.  
Email: [anatoly.kukk@hot.uni-hannover.de](mailto:anatoly.kukk@hot.uni-hannover.de)

## Funding information

Deutsche Forschungsgemeinschaft, Grant/Award Numbers: RO 3471/18-1, EM 63/13-1; German Research Foundation (DFG) under Germany's Excellence Strategy within the Cluster of Excellence PhoenixD, Grant/Award Number: EXC 2122, Project ID 390833453

## Abstract

We introduce a new single-head multimodal optical system that integrates optical coherence tomography (OCT), 18 MHz ultrasound (US) tomography and Raman spectroscopy (RS), allowing for fast (<2 min) and noninvasive skin cancer diagnostics and lesion depth measurement. The OCT can deliver structural and depth information of smaller skin lesions (<1 mm), while the US allows to measure the penetration depth of thicker lesions ( $\geq 4$  mm), and the RS analyzes the chemical composition from a small chosen spot ( $\leq 300$   $\mu\text{m}$ ) that can be used to distinguish between benign and malignant melanoma. The RS and OCT utilize the same scanning and optical setup, allowing for co-localized measurements. The US on the other side is integrated with an acoustical reflector, which enables B-mode measurements on the same position as OCT and RS. The US B-mode scans can be translated across the sample by laterally moving the US transducer, which is made possible by the developed adapter with a flexible membrane. We present the results on custom-made liquid and agar phantoms that show the resolution and depth capabilities of the setup, as well as preliminary ex vivo measurements on mouse models with  $\sim 4.3$  mm thick melanoma.



## KEYWORDS

multimodal setup, optical coherence tomography, Raman spectroscopy, skin cancer diagnostics, ultrasound

This is an open access article under the terms of the [Creative Commons Attribution](https://creativecommons.org/licenses/by/4.0/) License, which permits use, distribution and reproduction in any medium, provided the original work is properly cited.

© 2022 The Authors. *Journal of Biophotonics* published by Wiley-VCH GmbH.

## 1 | INTRODUCTION

The incidence of skin cancer has been rapidly increasing worldwide over the past decades, especially in countries with high sun exposure and population with Caucasian skin type. The rising incidence rates are most likely a consequence of the significant changes in leisure time behavior since the 20th century, for example, vacationing in areas with higher sun exposure and increasing exposure to ultraviolet (UV) radiation. People between 45 and 60 years are particularly affected. In the case of malignant melanoma, the most dangerous type of skin cancer with the highest mortality rate, the incidence rate has more than tripled in the last 3 decades. For example, in Germany, the risk of developing melanoma in the course of a lifetime is about 1:60, and the mortality risk is about 1:400 [1].

Melanoma is particularly dangerous, as it can be asymptomatic at early stages and its resemblance with benign moles makes it difficult to be discovered. By diagnosing and surgically removing melanoma in the early stages, full recovery chances are as high as 95%. However, untreated melanoma can reach blood vessels and metastasize to lymph nodes and organs, which leads to drastic decrease of the recovery chances to as little 10% [1, 2]. Therefore, early identification of melanoma is vital for the patient's outcome.

Currently, the diagnosis of skin cancer is based on the visual inspection of the lesion by the naked eye or with a dermoscope, followed by complete excision of the lesion and histological examination in case the lesion is considered suspicious by the dermatologist. Unfortunately, the visual inspection is error-prone, with reported false positives and false negative rates of  $\geq 20\%$  [3–5]. Furthermore, the depth of melanoma is another critical parameter that plays a role in the excision and it cannot be measured precisely by noninvasive dermoscopic examination. While it can be estimated with the Clark scale and Breslow thickness metrics, the precise thickness measurement is done by the histological examination of the sample, which is considered as the gold standard in diagnostics [6, 7]. However, the histology examines only a single two-dimensional (2D) slice of the lesion, which might not be positioned at the point of largest thickness, thus possibly underestimating the lesion depth.

If the dermatologist had a fast and noninvasive method to diagnose and measure skin lesion depth, several appointments and excisions would be reduced to a single one, as well as excisions for noncancerous nevi would no longer be necessary. Numerous studies have proposed and investigated noninvasive optical and ultrasound techniques for *in vivo* skin cancer measurement. For example, confocal and multiphoton microscopy (MPM) have been demonstrated to distinguish between benign and malignant lesions; they were found however limited by impractical penetration depth of  $\leq 200\ \mu\text{m}$  in pigmented skin [8–10].

Similarly, optical coherence tomography (OCT) was applied for the measurement of lesions with thickness  $\leq 500\ \mu\text{m}$  [11, 12]. For measurement of lesions with depths  $\geq 1\ \text{mm}$ , ultrasound with frequency  $\geq 15\ \text{MHz}$  has been demonstrated to show good agreement with histological results [13–17]. As for classification and diagnosis, Raman spectroscopy (RS) has been capable of distinguishing melanoma and benign skin lesions by analyzing lipid and melanin bands, additionally identifying different skin cancer types [18–23]. Finally, in the last years, numerous studies have emerged with multi- and hyperspectral imaging systems that are able to rapidly classify and predict benign and malignant lesions from the surface [24–27].

However, no single modality has the capacity to both diagnose the melanoma and measure its thickness over all possible ranges ( $50\ \mu\text{m}$ – $\geq 4\ \text{mm}$ ) noninvasively, which is why they are not established in clinical routine. A combination of these techniques could overcome their limitations and allow for a fast measurement and diagnosis of skin lesions. Although it is possible to apply different modalities one after another, it would be time consuming and due to switching of scanning units, there would be no guarantee that the imaging will be performed at the same positions, introducing a possible error source. As shown in Table 1, different setups for optical biopsy of melanoma were proposed, with the most common design integrating OCT and photoacoustics (PA). The extensive work that combines OCT and photoacoustical microscopy (PAM) is not considered here, since PAM delivers en-face images at a fixed depth and it is therefore difficult to be compared with OCT images. In addition, it currently requires long measurement times, unpractical for clinical applications. Since the combination of PA/US with OCT is complicated by the nontransparent (conventional) ultrasound device, the measurements with the two modalities are usually performed separately or the PA is obtained by using a Fabry-Perot interferometer (FPI). As the latter method involves scanning of the interrogation spot, it has the disadvantage of long acquisition times and high exposure that can exceed the maximal permissible exposure (MPE) levels for human skin.

In this work, we developed and tested a system that combines OCT, RS and US in a single scanning head. The OCT delivers information on upper skin structures as well as thickness measurement for thin lesions. The information from RS enables distinction between malignant lesions and noncancerous nevi. The RS is collected from a small ( $\leq 300\ \mu\text{m}$  diameter) spot that is steered with OCT galvoscaners. This not only allows to measure the spectra at precise indicated positions, excluding interference from neighboring normal skin areas, but also for several measurements at different positions. Finally, the ultrasound is achieved by adding a water-

TABLE 1 Survey of multimodal systems for optical biopsy of melanoma

Reference	Modalities	Acquisition time	Remarks
Zhang et al [28]	OCT, PAT	>7 min	• PAT with FPI
Meyer et al [16]	OCT, US	OCT: N.S.; US: 1-2 min	• US applied separately
Chen et al [29]	OCT, PAT	>8 min	• PAT with FPI
Mazurenka et al [30]; Varketin et al [31]	OCT, RS, PA	>2 min	• PA applied separately • PA only as one-dimensional depth profile
Kratkiewicz et al [32]	OCT, PAT, US	N.S.	• OCT applied as a separate unit
Park et al [33]	Multispectral PAT	~1 min	
Elagin et al [10]	Optical coherence angiography, MPM	<1 min	• MPM depth limited to 200 $\mu\text{m}$
Proposed setup	OCT, RS, US	<2 min	• Single scanning unit • Co-localized OCT, RS and US

Abbreviations: FPI, Fabry-Perot interferometer; MPM, multiphoton microscopy; N.S.: not specified; OCT, optical coherence tomography; PA, photoacoustic imaging; PAT, photoacoustic tomography; RS, Raman spectroscopy.

filled container with an acoustical mirror, that decouples the acoustical path from the main axis to the US transducer. By including a flexible membrane, the transducer and the acoustical mirror can be moved within the container, which allows translation of the B-mode measurement line and thus enables measurements at different positions without moving the sample. The capabilities of the presented setup are tested on agar phantoms and ex vivo mouse melanoma.

## 2 | MATERIALS AND METHODS

### 2.1 | Experimental setup

The schematic of the multimodal setup is shown in Figure 1. It is the next-stage development of a previously demonstrated OCT-RS probe used in skin cancer screening [30]. The OCT is a spectral-domain OCT (GAN621, Thorlabs, USA) at a central wavelength of 900  $\mu\text{m}$  with a customizable probe head (OCTP-900) that was modified to include a coaxial RS collection system. The OCT signal (red path) is delivered from the base unit to the setup via fiber, where it is split into reference and sample arm. The sample signal is steered with a 2D galvoscaners M1 to M2 system and focused onto the sample with a focusing objective FO (fl = 36 mm, OCT-LK3-BB, Thorlabs, USA). Since the galvo mirror M2 partially transmits visible light, the scanning unit allows for simultaneous visualization of the sample plane by projecting (blue path) the latter onto a CC camera chip, after filtering out the laser light with a long pass filter LP1 at 550 nm (50NM 12.5MM, Edmund Optics Ltd, UK). Using resolution targets, the lateral and axial resolution in air of the OCT system is measured at 4 and 3  $\mu\text{m}$ , respectively.

The excitation for RS is done by using a frequency-doubled Nd:YAG laser (Ultra50, Quantel Laser, France) that emits pulses at 532 nm at 20 Hz repetition rate and 7 ns pulse duration. The pulses (green path) are guided via a 910  $\mu\text{m}$  core fiber (MPH910L02, Thorlabs, USA), cleaned from luminescence and the Raman signal from the fiber with a 4 nm narrow bandpass filter LF (FLH05532-4, Thorlabs, USA) and collimated with a 40 mm lens (LB4700, Thorlabs, USA).

The Raman signal (yellow path), which is mostly in the VIS range, is collected by the FO and decoupled from the OCT signal with a dichroic mirror DM (DMLP805R, Thorlabs, USA), with edge wavelength at 805 nm. The 532 nm longpass filter LP2 (RazorEdge ultrastep LP Edge filter, Semrock Inc., USA) and 700 nm shortpass filter SP (FESH0700, Thorlabs, USA) remove the Rayleigh (532 nm excitation) line and the OCT spectrum\* from the Raman signal before it is focused with a 60 mm focusing lens FL2 onto fiber bundle (LLB536-IR-0,22-1, Quantum Design GmbH, Germany) and sent to a 19 mm focal length spectrometer (Kymera 193i, Andor Technology Ltd, UK) equipped with CCD camera (iDus-LDC-DD, Andor Technology Ltd, UK) and a grating with 1200 L/mm with 600 nm blaze. A single RS measurement is performed with 10 s exposure time and 2.4 mJ per pulse, which translates in 5 mJ/cm<sup>2</sup> per pulse, which is allowed under the regulated MPE levels for human skin in vivo [34].

The US imaging is done with a single crystal 18 MHz UST transducer (L22-14vXLF, Vermon, France). This transducer has 128 elements, -6 dB bandwidth of 67% and an elevation pitch (acoustical focal length) of 20 mm, which corresponds to the total acoustical path distance to the sample. The transducer is connected to a research ultrasound system (Vantage 32 LE, Verasonics, USA) via a

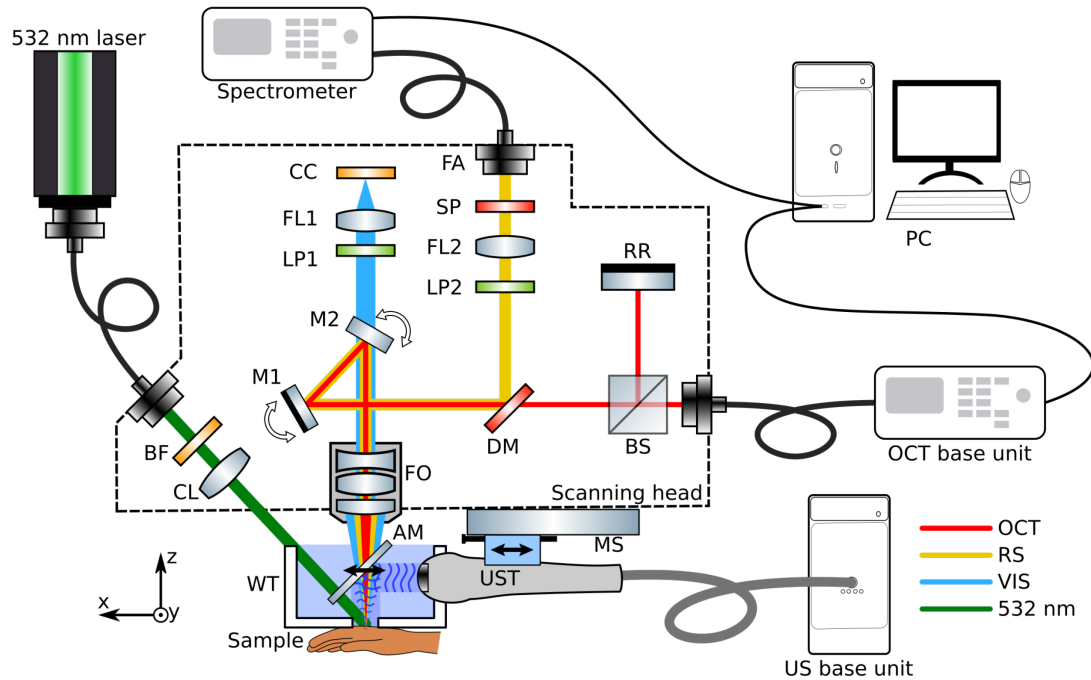


**FIGURE 1** Sketch of the experimental setup. AM, acoustical mirror; BF, bandpass filter; BS, beam splitter; CC, camera chip; CL, collimating lens; DM, dichroic mirror; FA, fiber adapter; FL, focusing lens; FO, focusing objective; LP, long pass filter; M, galvo mirrors; MS, motorized stage; OCT, optical coherence tomography; RR, retroreflector; SP, shortpass filter; UST, ultrasound transducer; WT, water tank. The lines represent the optical paths of OCT (red); RS collection (yellow); visible path for camera (blue) and the 532 nm excitation beam (green). The US creates a B-mode image in the yz plane; by translating the UST together with the AM in x direction the imaging can be performed at different planes

Universal Transducer Adapter (UTA 260-MUX, Verasonics, USA). The sampling is done at 62.5 MHz, which allows to fully cover the transducer bandwidth. The transducer itself is attached to a motorized stage MS (MTS25/M-Z8, Thorlabs, USA) that allows translation with respect to the scanning head in x direction (perpendicular to plane of B-mode), allowing for US imaging at defined positions without moving the sample.

To ensure that OCT and US perform the measurements on the same position, a self-made water tank (WT) with UST adapter attachment is designed and printed on a commercial 3D printer with acrylonitrile butadiene styrene (ABS), as shown in Figure 2. The acoustical path is folded by placing a 1 mm thick microscope glass slide at 45° angle that is carried by the UST adapter. Due to a large acoustical impedance mismatch between glass and water, the US waves are reflected and can be decoupled from the optical path.

The scanning head (marked with the dashed line in Figure 1, including the WT) is approximately  $24 \times 20 \times 20$  cm<sup>3</sup> and weighs under 6 kg. The measurements with the system are performed as follows: first, the WT is positioned on top of the sample. The UST with the AM are moved out of the optical path, so that the OCT and RS measurements can be performed dispersion-free through air. Then, the WT is filled with tap water and US measurements are performed. The acquisition time of the

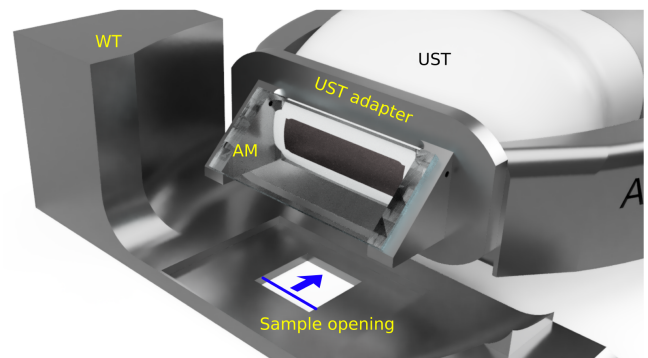


**FIGURE 2** Three-dimensional (3D) sketch of the US adapter and WT. A self-designed adapter is placed on the UST, that carries the acoustical mirror AM (glass slide at 45°) which reflects the US waves downwards. The sample is placed under the  $7 \times 7$  mm<sup>2</sup> opening at the bottom of the water tank. A single US B-mode image is done across the marked blue line. The rear side of the WT is sealed with flexible nitrile membrane, which allows for translation of the UST together with the AM in the direction of the blue arrow, enabling B-mode imaging at different positions. The front side of the WT is sealed with a glass slide. The glass slide, nitrile membrane and right wall of the WT are not represented for simplification and better visibility. AM, acoustical mirror; UST, ultrasound transducer; WT, water tank

presented trimodal system depends on the desired resolution and the size of the measurement area; a typical measurement on a skin area of  $7 \times 7$  mm<sup>2</sup> area requires less

than 2 minutes in total, consisting of 10 seconds for the RS measurement, 22 seconds for the OCT measurement with  $10\ \mu\text{m}$  lateral pixel size and 1 minute for the US measurement of 50 sections with spatial separation of  $150\ \mu\text{m}$  between them.

## 2.2 | Phantoms

The capabilities of the multimodal device are demonstrated with human hair positioned in suspended mode at increasing depths. For this purpose, a phantom mold is designed and printed with a commercial resin 3D printer. The mold has a  $4.3^\circ$  oblique side with notches every 2 mm, which allows to position strings at depths until 2.5 mm, with depth increments of  $150\ \mu\text{m}$ . The hair thickness varies between 56 and  $99\ \mu\text{m}$ . Imaging of the suspended samples was done in three variations: in air (with OCT only), in deionized water and in agar phantom, which is often used as tissue-mimicking phantoms for ultrasound and photoacoustic imaging [35–37].



**FIGURE 3** Photograph of the agar phantom inside the Three-dimensional (3D) printed mold. The human hairs inside the phantom are fixed with scotch tape and positioned at increasing depths with steps of  $150\ \mu\text{m}$

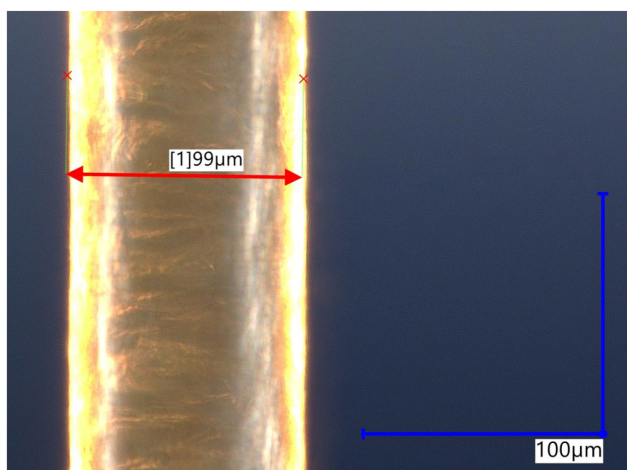


**FIGURE 4** Measurement of the RS spot size. Left: Microscope image of a single hair positioned inside the phantom mold, with its corresponding manual thickness measurement. Right: the corresponding measured Raman signal intensity by translating the collection focal point across a  $99\ \mu\text{m}$  thick hair in air. The signal is integrated from 2000 until  $3000\ \text{cm}^{-1}$  range. The red shaded area represents the hair position and thickness

The agar phantoms were prepared by bringing 100 mL of deionized water to  $60^\circ$  temperature inside an Erlenmeyer flask with magnetic stirring and adding 2 g of agar powder (A1296, Merck KGaA, Germany). The solution was brought and kept at  $80^\circ$  temperature for 5 minutes and injected into the mold. The upper part of the mold is covered with a microscope slide, thus creating a smooth top surface. A photograph of the prepared agar phantom with suspended hairs is shown in Figure 3.

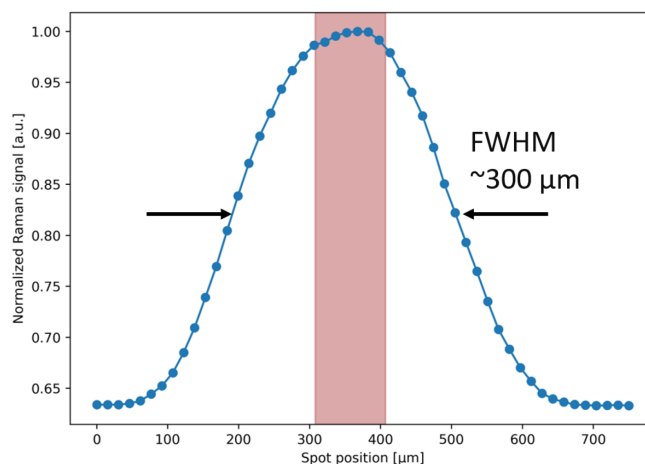
## 2.3 | Mouse melanoma

The proposed multimodal setup was validated ex vivo on a mouse model with developed melanoma. An adult C57/BL6 mouse (HgfXCdk4 type) was injected with transplantable HcMel12 melanoma cell line, that has been established from a spontaneous melanoma of an Hgf-Cdk4 R24C mouse [38, 39]. The mouse was sacrificed on day 24 after the injection and the skin tissues around the developed melanoma is excised and measured with the multimodal setup. After measurements with the setup, the sample is embedded in 10% formalin solution for histological examination of hematoxylin-eosin stained slices.

## 3 | RESULTS AND DISCUSSION

### 3.1 | Phantoms

First, the size of the RS collection spot is measured by translating the focal point across a  $99\ \mu\text{m}$  thick hair in steps of  $15\ \mu\text{m}$ . For each measurement, the RS signal



intensity is integrated across the 2000 to 3000  $\text{cm}^{-1}$  range. The results are shown in Figure 4. By measuring the full width at half maximum (FWHM), the diameter of the RS collection is  $\leq 300 \mu\text{m}$ . While this value is larger than some of the reported joint OCT-RS systems [40], it is small enough to be positioned on small lesions and confine the RS measurements to that point without collecting signal from the neighboring tissue, which would complicate the dignity diagnosis. Also, for larger lesions, a reasonable sampling can be realized to differentiate between different spots.

As shown with the exemplary results in Figure 5, the OCT is capable of resolving strands in approximately 1.5 mm depth in a single measurement in air, and  $\leq 700 \mu\text{m}$  in water and agar phantoms, the latter due to light scattering and shorter optical path caused by refraction. The US is capable of resolving all the strands, thus, its maximal penetration depth can be considered as at least 4 mm, which is sufficient to resolve the invasion depths of many melanomas. The presented design however cannot be used for measurement of the lateral or axial resolution of the modalities, since for both OCT and US the hair samples are imaged as two horizontal lines (instead of a singular point) due to the reflections at the interfaces.

The described agar phantom offers potential for more complex models. For instance, by creating multi-layered agar phantoms with different scattering and absorbing parameters a better resemblance to skin tissue can be achieved, as demonstrated in other works [36, 41]. In addition, by soaking the hair strands in dyes with known

RS response and measuring the signal from strands at increasing depths, the axial limits of the RS modality can be investigated.

### 3.2 | Mouse samples

For RS measurements, the signal is collected on the central position of melanoma and on the adjacent healthy tissue, at the positions indicated in Figure 6 with red and green crosses. The baseline of the raw spectra is first removed using iterative morphological and mollifier-based algorithms to eliminate the fluorescence background [42]. After that, the spectra are normalized and smoothed for a more intuitive comparison. The post-processed spectra are presented in Figure 6. In the fingerprint spectral range, some characteristic peaks of biological Raman spectra are clearly displayed, such as the protein vibration bands at 1260 and 1660  $\text{cm}^{-1}$  (attributed to Amide-III and Amide-I bands) and the lipid vibration bands at 1100, 1310, and 1440  $\text{cm}^{-1}$  (corresponding to C–C stretch, CH<sub>2</sub> twist and CH<sub>2</sub>–CH<sub>3</sub> bands, respectively). More importantly, an obvious difference is that at 1565  $\text{cm}^{-1}$  (marked with a black straight line in the figure), the peak intensity of melanoma is significantly higher than that of normal skin, which is consistent with the research of Huang et al who found that this peak is the characteristic of melanin [19]. In the water band range, compared to the healthy tissue spectrum, the melanoma spectra present stronger and better-defined RS peaks at 2876  $\text{cm}^{-1}$ , 2934  $\text{cm}^{-1}$  and in

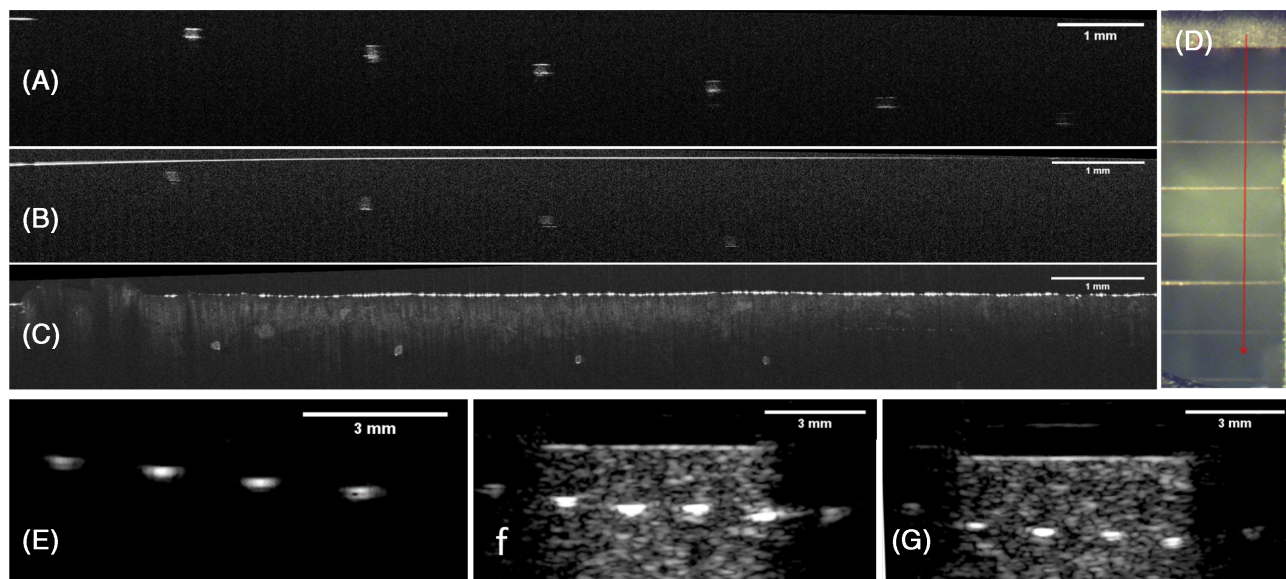
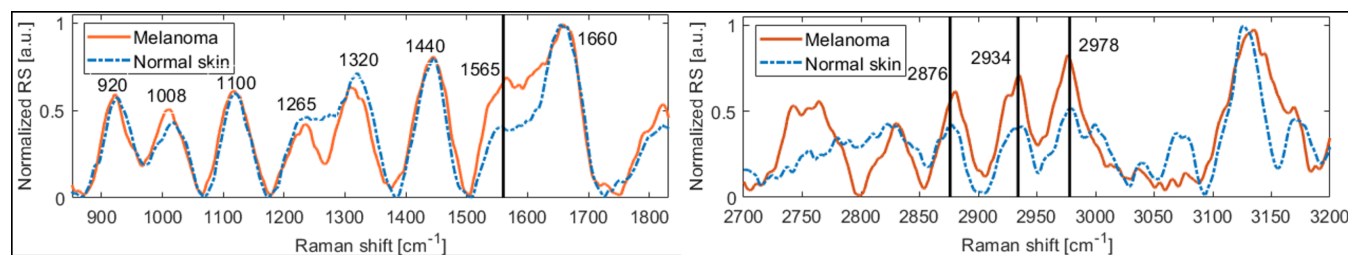
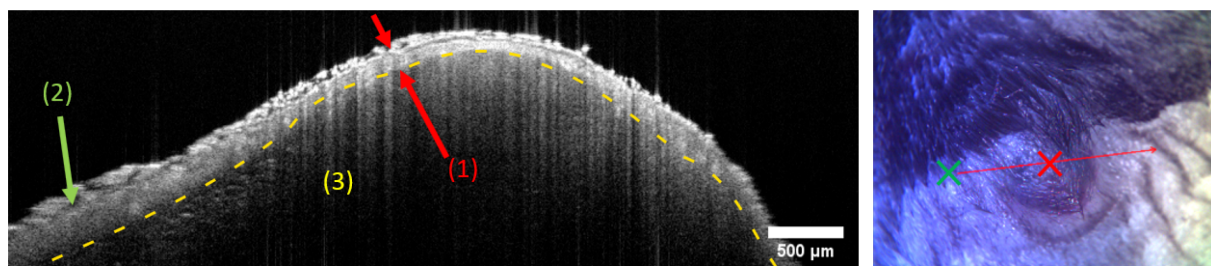


FIGURE 5 Exemplary results of optical coherence tomography (OCT) and ultrasound (US) measurements on hair strands. (A–C) are the OCT measurements in air, water and agar phantom; (D) shows the visible camera image from the top and the OCT measurement line in air (red). (E,F) are the US measurements on water and agar samples; (g) shows the hair strands at larger depths of  $\geq 3 \text{ mm}$



**FIGURE 6** Raman spectroscopy (RS) measurement of mouse skin sample. Left: Spectra at melanoma position (orange) and adjacent healthy skin (blue dash-dot line) in the finger print range ( $800\text{--}1800\text{ cm}^{-1}$ ), right: in the water band range ( $2700\text{--}3200\text{ cm}^{-1}$ ). The spectra have been post-processed with baseline correction, normalization and smoothed. The black vertical lines represent the relevant peak lines



**FIGURE 7** Optical coherence tomography (OCT) scan of the mouse melanoma. Left: exemplary OCT scan, with (1) marking the distinctive dermal layer above the melanoma, (2) marking the dermis at the normal skin and (3) indicating the melanoma, with yellow line representing its upper boundary. Right: the corresponding camera image and the OCT measurement line. The green and red crosses indicate the positions for measurement of RS from Figure 6. Note the similarity of the dermal layer structure with the histological measurement of this sample, shown in Figure 9

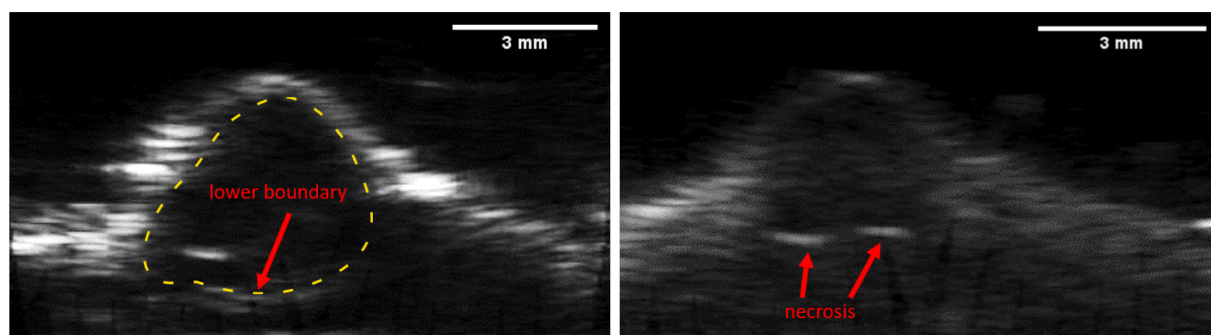


**FIGURE 8** Exemplary ultrasound (US) B-scans of mouse melanoma. Left: scan that captures the lower boundary of the melanoma at depth of approximately  $4.3\text{ mm}$ . The yellow dash line marks the shape of the melanoma. Right: scan that reveals two highly scattering positions at a depth of  $2.7\text{ mm}$ , which are attributed to internal necrosis spots, see Figure 9

particular,  $2978\text{ cm}^{-1}$ . Other RS studies on human skin cancer also report an increased RS signal at these vibrational frequencies, which are attributed to the C–H stretching modes of proteins and lipids [18, 43].

The OCT measurements on the mouse melanoma are shown in Figure 7. The dermal layer around the melanoma position presents a particularly high-contrast layered structure with thickness of  $96 \pm 10\ \mu\text{m}$ . In comparison, the measurements on healthy tissue yield a rather thick homogeneous layer. This structure and the thickness agree

well with the corresponding histological measurement, shown in Figure 9. Hematoxylin-eosin staining shows a circumscribed dermal proliferation of malignant melanocytic cells with patchy pigment deposits and focal necrosis and hemorrhage.

The US measurements of the mouse samples are shown in Figure 8, which demonstrates the circular shape and the lower boundary of the melanoma at a depth of approximately  $4.3\text{ mm}$ . At several positions the B-scans measured highly scattering inclusions  $1\text{ mm}$  wide at a depth of

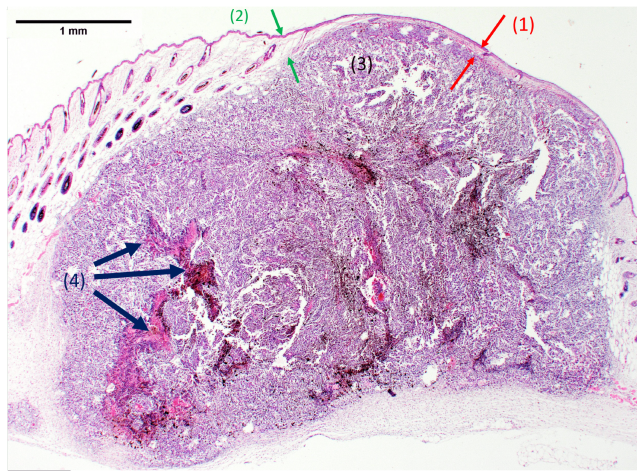


**FIGURE 9** Histological measurement of the mouse melanoma. The Raman spectroscopy (RS) of this sample is demonstrated in Figure 6, of optical coherence tomography (OCT) in Figure 7 and of US in Figure 8. (1) indicates the particular dermal structure above the tumor that is captured with OCT/US, (2) shows the thicker healthy skin, (3) is the melanoma and (4) points at internal necrotic areas located at the bottom of melanoma, which is recorded with the US

2.7 mm, which are attributed to the necrotic areas that can be seen in the subsequent histological measurement.

## 4 | DISCUSSION

The histology of the mouse melanoma agrees well with the OCT and US results in terms of dermal structure, which is particularly thin and pronounced above the melanoma and thicker on healthy tissue. OCT and histology yield  $92 \pm 10$  and  $81 \pm 19$   $\mu\text{m}$ , respectively, when manually measuring the thickness at several positions. As shown in Figures 7 and 9, the dermal structure on the left side of the melanoma becomes more homogeneous and thickens rapidly, which is also visible on US imaging. The thickness of this layer is measured at  $665 \pm 112$   $\mu\text{m}$  with US and  $618 \pm 74$   $\mu\text{m}$  with histology. The longest diagonal is used to determine the maximum depth of melanoma. The US thickness is  $5.4 \pm 0.25$  mm, which agrees with the histological value of  $5.1 \pm 0.1$  mm when the FWHM of the upper boundary is taken into account. In general, the histological measurements are lower, and the circular shape of melanoma is distorted. This can be attributed to tissue shrinkage, as dehydration and paraffinization of the tissue are known to cause tissue deformations [44].

Combined with the phantom measurements, we believe that the proposed multimodal setup is capable of delivering RS and depth information that can assist the dermatologist in the diagnosis of the potential skin

cancer, as well in the decision for excision margins. Future work will be directed towards further integration and automation as well as increase in measurement accuracy and spectral resolution. Ultimately, pre-clinical tests will be conducted to assess the in vivo capabilities. For clinical measurements, the dimensions and the weight of the scanning unit are well-suited to be mounted on a commercial articulated gas spring monitor arm. The arm itself is installed on the table that carries the PC and the rest of the remaining components, for example, the laser, OCT and US base units. This setup allows for easier positioning of the scanner opening, which is then pressed against the skin lesion, reducing possible motion artifacts. For smaller lesions, the imaged area and time can be reduced, decreasing artifact further. In the current setup, the dimensions of the WT and its opening are limiting the application on rather open and accessible body parts, which can be solved by modifying it to feature a narrow conical shape.

In future studies, it is intended to add the PA modality to the setup, as it already integrated a pulsed laser source and the US system. PA has already been used in skin cancer-related studies [31, 33, 45, 46]. Unlike US, which delivers information based on acoustical reflectivity of the sample, PA provides contrast based on optical absorption of the tissue. This information can be important in cases where the US contrast between melanoma and surrounding tissues is low due to the similar acoustical impedance. This has been demonstrated in our previous results on layered polyvinyl alcohol-based hydrogel phantoms, which also showed good correlation with numerical simulations [47–49]. By replacing the excitation laser with a tunable laser system such as an optical parametric oscillator (OPO), so-called PA spectrometry can be added to the modalities, which expands the PA information by providing absorption information at different wavelengths [50]. The excitation at different wavelengths would also amplify the RS modality, allowing additional information on chemical composition.

## 5 | CONCLUSIONS

We have developed a multimodal imaging system that integrates OCT and US in a single scanning unit allowing for structural and depth measurement of skin lesions as well as RS measurements with the goal to enable noninvasive diagnosis of skin cancer. Compared to other multimodal OCT-US systems that measure only a single plane, our proposed design involves an acoustical reflector that is mounted on an adapter, allowing for co-localized OCT, RS and US measurements. For proof of principle, the multimodal setup was validated on hair strands fixated at



different depths inside water and agar phantoms, which showed the maximal penetration depth of OCT at  $\leq 700 \mu\text{m}$  inside water and agar phantoms. The maximal US depth is at least 4 mm, which is sufficient for the depth resolution of most skin lesions. Finally, the multi-modal setup is tested on a mouse melanoma sample, where RS showed a difference in signal from healthy tissue and melanoma, while OCT and US measured dermal structure and melanoma depth that correlated well with the histology. Future work will focus on adding an OPO as excitation source and PA tomography and spectrometry, which will allow for additional information on the skin for more precise diagnosis.

## ACKNOWLEDGMENT

Open Access funding enabled and organized by Projekt DEAL.

## FUNDING INFORMATION

The authors acknowledge financial support from the German Research Foundation DFG (German Research Foundation, Project ID RO 3471/18-1 and EM 63/13-1). Also, financial support from the German Research Foundation (DFG) under Germany's Excellence Strategy within the Cluster of Excellence PhoenixD (EXC 2122, Project ID 390833453) is acknowledged.

## CONFLICTS OF INTEREST

The authors declare no potential conflict of interests.

## DATA AVAILABILITY STATEMENT

The data that support the findings of this study are available from the corresponding author upon reasonable request.

## ORCID

Anatoly Fedorov Kukk  <https://orcid.org/0000-0003-2233-4960>

Bernhard Roth  <https://orcid.org/0000-0001-9389-7125>

## ENDNOTES

\* Some internal back reflections of the OCT signal reach the CCD camera avoiding the grating and contaminating the spectrum, thus, requiring the shortpass filter.

† Although it is possible to resolve deeper structures by manually adjusting the reference arm length, this strategy is not followed in this work.

## REFERENCES

- [1] B. Barnes, K. Kraywinkel, E. Nowossadeck, I. Schönfeld, A. Starker, A. Wienecke, U. Wolf, *Bericht zum Krebsgeschehen in Deutschland 2016*, Robert Koch-Institut, Berlin **2016**.
- [2] T. Wang, J. Qiu, T. E. Milner, *Skin Cancer Overview* **2011**, 1, 109.
- [3] M. E. Ming, *J. Am. Acad. Dermatol.* **2000**, 43(4), 704.
- [4] P. Carli, F. Mannone, V. De Giorgi, P. Nardini, A. Chiarugi, B. Giannotti, *Melanoma Res.* **2003**, 13(2), 179.
- [5] V. Papageorgiou, Z. Apalla, E. Sotiriou, C. Papageorgiou, E. Lazaridou, S. Vakirlis, D. Ioannides, A. Lallas, *J. Eur. Acad. Dermatol. Venereol.* **2018**, 32(6), 879.
- [6] R.-M. Szeimies, A. Hauschild, C. Garbe, et al., *Tumoren der Haut: Grundlagen, Diagnostik und Therapie in der dermatologischen Onkologie*, Georg Thieme Verlag, Stuttgart **2010**.
- [7] H. D. Heibel, L. Hooey, C. J. Cockerell, *Am. J. Clin. Dermatol.* **2020**, 21(4), 513.
- [8] E. Yew, C. Rowlands, P. T. C. So, *J. Innovative Opt Health Sci* **2014**, 7(5), 1330010.
- [9] S. K. T. Que, *J. Investigative Dermatol* **2016**, 136(4), e33.
- [10] V. Elagin, E. Gubarkova, O. Garanina, D. Davydova, N. Orlinskaya, L. Matveev, I. Klemenova, I. Shlivko, MShirmanova, E. Zagaynova, *Sci Rep* **2021**, 11(1), 1.
- [11] A. Varkentin, M. Mazurenka, E. Blumenröther, M. Meinhardt-Wollweber, M. Rahlves, S. M. C. Broekaert, S. Schäd-Trcka, S. Emmertinst, U. Morgner, B. Roth, *J Biophotonics* **2017**, 10(6–7), 854.
- [12] M. Rahlves, M. Mazurenka, A. Varkentin, E. Blumenroether, J. Stritzel, U. Morgner, M. Meinhardt-Wollweber, S. Schäd-Trcka, S. Emmert, B. Roth, in *The European Conference on Lasers and Electro-Optics*, Munich, Germany, June **2017**, p. JSIII\_2\_3.
- [13] G. Pellacani, S. Seidenari, *Arch. Dermatol.* **2003**, 139(3), 293.
- [14] P. Guitera, L. X. Li, K. Crotty, P. Fitzgerald, R. Mellenbergh, G. Pellacani, S. W. Menzies, *Br. J. Dermatol.* **2008**, 159(2), 364.
- [15] I. Fernández Canedo, M. de Troya Martín, R. Fúnez Liébana, F. Rivas Ruiz, G. Blanco Eguren, N. Blázquez Sánchez, *Actas Dermo-Sifiliográficas (English Edition)* **2013**, 104(3), 227.
- [16] N. Meyer, V. Lauwers-Cances, S. Lourari, J. Laurent, M. P. Konstantinou, J.-M. Lagarde, B. Krief, H. Batatia, L. Lamant, C. Paul, *Br. J. Dermatol.* **2014**, 171(4), 799.
- [17] C. M. Botar-Jid, R. Cosgarea, S. D. Bolboacă, S. C. Şenilă, L. M. Lenghel, L. Rogojan, S. M. Ducea, *Am. J. Roentgenol.* **2016**, 206(4), 699.
- [18] M. Gniadecka, P. A. Philipsen, S. Sigurdsson, S. Wessel, O. F. Nielsen, D. H. Christensen, J. Hercogova, K. Rossen, H. K. Thomsen, R. Gniadecki, L. K. Hansen, H. C. Wulf, *J. Invest. Dermatol.* **2004**, 122(2), 443.
- [19] Z. Huang, L. Harvey, X. K. Chen, A. Alajlan, D. I. McLean, H. Zeng, *J. Biomed. Opt.* **2004**, 9(6), 1198.
- [20] S. Tfaili, C. Gobinet, G. Josse, J.-F. Angiboust, M. Manfait, O. Piot, *Analyst* **2012**, 137(16), 3673.
- [21] P. A. Philipsen, L. Knudsen, M. Gniadecka, M. H. Ravnbak, H. C. Wulf, *Photochem. Photobiol. Sci.* **2013**, 12(5), 770.
- [22] X. Feng, A. J. Moy, H. T. M. Nguyen, Y. Zhang, J. Zhang, M. C. Fox, K. R. Sebastian, J. S. Reichenberg, M. K. Markey, J. W. Tunnell, *J. Biomed. Opt.* **2018**, 23(5), 057002.
- [23] M. Wollweber, B. Roth, *Sensors* **2019**, 19(10), 2387.
- [24] L. Rey-Barroso, F. J. Burgos-Fernández, X. Delpueyo, M. Ares, S. Royo, J. Malvehy, S. Puig, M. Vilaseca, *Sensors* **2018**, 18(5), 1441.
- [25] L. Rey-Barroso, F. J. Burgos-Fernández, M. Ares, S. Royo, X. Delpueyo, S. Puig, J. Malvehy, G. Pellacani, M. Vilaseca, in *European Conference on Biomedical Optics*, Munich, Germany, June **2019**, p. 11073\_10.
- [26] R. Leon, B. Martinez-Vega, H. Fabelo, S. Ortega, V. Melian, I. Castaño, G. Carretero, P. Almeida, A. Garcia, E. Quevedo, J. A. Hernandez, B. Clavo, G. M. Callico, *J. Clin. Med.* **2020**, 9(6), 1662.

- [27] S. Bozsányi, N. N. Varga, K. Farkas, A. Bánvölgyi, K. Lőrincz, I. Lihacova, A. Lihachev, E. V. Plorina, Á. Bartha, A. Jobbágy, et al., *J. Clin. Med.* **2022**, *11*(1), 189.
- [28] E. Z. Zhang, B. Povazay, J. Laufer, A. Alex, B. Hofer, B. Pedley, C. Glittenberg, B. Treeby, B. Cox, P. Beard, et al., *Biomed. Opt. Express* **2011**, *2*(8), 2202.
- [29] Z. Chen, E. Rank, K. M. Meiburger, C. Sinz, A. Hodul, E. Zhang, E. Hoover, M. Minneman, J. Ensher, P. C. Beard, et al., *Sci. Rep.* **2017**, *7*(1), 1.
- [30] M. Mazurenka, L. Behrendt, M. Meinhardt-Wollweber, U. Morgner, B. Roth, *Rev. Sci. Instruments* **2017**, *88*(10), 105103.
- [31] A. Varkentin, M. Mazurenka, E. Blumenröther, L. Behrendt, S. Emmert, U. Morgner, M. Meinhardt-Wollweber, M. Rahlves, B. Roth, *J. Biophotonics* **2018**, *11*(6), e201700288.
- [32] K. Kratkiewicz, R. Manwar, A. Rajabi-Estarabadi, J. Fakhoury, J. Meiliute, S. Daveluy, D. Mehregan, K. M. Avanaki, *Sensors (Basel, Switzerland)* **2019**, *19*(12), 2815.
- [33] B. Park, C. H. Bang, C. Lee, J. H. Han, W. Choi, J. Kim, G. S. Park, J. W. Rhie, J. H. Lee, C. Kim, *J. Eur. Acad. Dermatol. Venereol.* **2021**, *35*(3), 669.
- [34] America Llo, Laser Institute of America, Orlando, Florida **2014**.
- [35] R. M. Souza, T. Q. Santos, D. P. Oliveira, A. V. Alvarenga, R. P. B. Costa-Felix, *J. Phys.: Conf. Series* **2016**, *733*, 012044.
- [36] A. Mustari, I. Nishidate, M. A. Wares, T. Maeda, S. Kawachi, S. Sato, M. Sato, Y. Aizu, *J. Visualized Exp.* **2018**, *138*, e57578.
- [37] L. Ntombela, B. Adeleye, N. Chetty, *Heliyon* **2020**, *6*(3), e03602.
- [38] J. Landsberg, E. Gaffal, M. Cron, J. Kohlmeyer, M. Renn, T. Tüting, *Pigment Cell Melanoma Res.* **2010**, *23*(5), 649.
- [39] D. Tormo, A. Ferrer, E. Gaffal, J. Wenzel, E. Basner-Tschakarjan, J. Steitz, L. C. Heukamp, I. Gütgemann, R. Buettner, M. Malumbres, et al., *Am. J. Pathol.* **2006**, *169*(2), 665.
- [40] X. Ren, K. Lin, C.-M. Hsieh, L. Liu, X. Ge, Q. Liu, *Biomed. Opt. Express* **2022**, *13*(1), 344.
- [41] A. I. Chen, M. L. Balter, M. I. Chen, D. Gross, S. K. Alam, T. J. Maguire, M. L. Yarmush, *Medical physics* **2016**, *43*(6Part1), 3117.
- [42] M. Koch, C. Suhr, B. Roth, M. Meinhardt-Wollweber, *J. Raman Spectros.* **2017**, *48*(2), 336.
- [43] C.-h. Liu, B. Wu, L. A. Sordillo, S. Boydston-White, V. Sriramoju, C. Zhang, H. Beckman, L. Zhang, Z. Pei, L. Shi, et al., *J. Cancer Metas. Treatment* **2019**, *5*, 4.
- [44] A. A. Plekhanov, M. A. Sirotkina, A. A. Sovetsky, E. V. Gubarkova, S. S. Kuznetsov, A. L. Matveyev, L. A. Matveev, E. V. Zagaynova, N. D. Gladkova, V. Y. Zaitsev, *Sci. Rep.* **2020**, *10*(1), 1.
- [45] U. Dahlstrand, R. Sheikh, A. Merdasa, R. Chakari, B. Persson, M. Cinthio, T. Erlöv, B. Gesslein, M. Malmjö, *Photoacoustics* **2020**, *18*, 100187.
- [46] A. Fedorov Kukk, E. Blumenröther, B. Roth, *Biomed. Phys. Eng. Exp.* **2022**, *8*(3), 035029.
- [47] E. Blumenröther, O. Melchert, M. Wollweber, R. Bernhard, *Photoacoustics* **2016**, *4*(4), 125.
- [48] O. Melchert, E. Blumenröther, M. Wollweber, B. Roth, *Eur. Phys. J. D* **2018**, *72*(1), 1.
- [49] E. Blumenröther, O. Melchert, J. Kanngießner, M. Wollweber, B. Roth, *Sensors* **2019**, *19*(9), 2195.
- [50] T. Lucas, M. Sarkar, Y. Atlas, C. Linger, G. Renault, F. Gazeau, J. Gateau, Calibrated Photoacoustic Spectrometer Based on a Conventional Imaging System for in Vitro Characterization of Contrast Agents. arXiv [physics.ins-det] 2020. <https://doi.org/10.48550/ARXIV.2003.08805>.

**How to cite this article:** A. Fedorov Kukk, D. Wu, E. Gaffal, R. Panzer, S. Emmert, B. Roth, J. *Biophotonics* **2022**, *15*(10), e202200129. <https://doi.org/10.1002/jbio.202200129>